JOURNAL OF AIRCRAFT
Vol. 46, No. 6, November–December 2009

Computational Study of Flexible Wing Ornithopter Flight

Beatrice Roget* and Jayanarayanan Sitaraman†
University of Wyoming, Laramie, Wyoming 82071
and
Robyn Harmon,‡ Jared Grauer,§ James Hubbard,¶ and Sean Humbert**
University of Maryland, College Park, Maryland 20742

DOI: 10.2514/1.43187

This paper presents the development and evaluation of a computational fluid dynamics based methodology to predict the aerodynamic forces produced by a flexible flapping wing. The computational fluid dynamics analysis code solves the compressible Reynolds-averaged form of the Navier–Stokes equations on structured curvilinear grids. A grid deformation algorithm is devised that deforms the body-conforming volume grid at each time step consistent with the measured wing motions. This algorithm is based on geometric considerations and is both computationally efficient and capable of handling very large deformations. This methodology is validated using experimental data obtained from a test on an ornithopter with flexible wings. Test data include measurements of the wing surface deformations as well as the generated forces in the horizontal and vertical directions. Correlation with test data shows good agreement with measured vertical force and satisfactory agreement with measured horizontal force at low flapping frequencies. However, the prediction accuracy degrades with an increase in flapping frequency. Evidence of resonance in the vehicle system was detected from the analysis of the experimental data. Unmodeled inertial effects from the vehicle body and support mounts may be one of the contributors to disagreement between the data and analysis.

I. Introduction

SEVERAL ornithopter designs currently exist that show varied degrees of success, but with flight qualities still very inferior to the level of control and agility associated with natural bird flight. One reason for the poor performance is the lack of understanding of the fundamental physical mechanisms behind flapping wing flight. Computations and experiments have been conducted in the past for rigid and moderately flexible wings with various motion profiles [1–4]. A comprehensive review of the various experimental and numerical investigations on flapping wing flight can be found in [5,6]. Although these studies are very insightful, further investigations are required to gain a complete understanding of the complex aerodynamic phenomena during actual bird flight.

An analysis tool capable of accurate predictions of aerodynamic and structural dynamic loading is a necessity for optimizing the wing shape and wing dynamics for future ornithopter designs. Modeling the physics of flapping wing flight is multidisciplinary in nature and requires a strong coupling between fluid and structural solution procedures. The objective of this paper is to focus on the first part of the problem and develop, evaluate, and validate a computational fluid dynamics (CFD) based methodology for prediction of the aerodynamic loading on flexible flapping wings. Any multidisciplinary analysis methodology requires a thorough evaluation of tools representing individual disciplines before they can be interfaced together into a comprehensive analysis. Therefore, experimental data that facilitate systematic decoupling and validation of a multiphysics problem are very valuable. The motivation of the current work stems from such an experiment conducted by University of Maryland researchers [7] on an ornithopter design. This experiment provides measurements of both wing deformations as well as total forces, thus forming a rich source for validation of the CFD methodology. The measured aeroelastic motions can be prescribed in the CFD methodology and used to compute the aerodynamic loading. The predicted aerodynamic loading can then be correlated with the force data to quantify the reliability and accuracy of the CFD method. In addition, the flowfield computed by the CFD methods can be probed to improve understanding of the aerodynamic mechanisms of flexible wing flapping.

Accurate CFD prediction of avian flight with flexible wings presents many difficult challenges, such as large elastic grid deformations and the possibility of laminar-to-turbulent transition. The present study addresses the former aspect and focuses on the development of a methodology to solve the Navier–Stokes equations around a highly flexible wing. To simulate the flow around very flexible wings using body-conforming meshes, a method must be devised to deform the volume mesh at each time step. It should be noted that CFD methods such as the immersed boundary method [8–10] and the particle vortex method [1] (which is meshless) do not require explicit volume grid deformation schemes. However, these CFD methods have only been extensively tested for very low Reynolds number problems. Currently, there are two common methods to solve the mesh deformation problem: the spring analogy method and the elastic body analogy method. In the spring analogy method [11], each node of the CFD grid is connected to its neighbor by springs and the equations of motion are integrated in time to compute the deformed grid position. This method can easily lead to grid invalidity for large motions. An improvement to the method [12] also considers torsional springs to avoid grid invalidity problems; however, this increases the computational cost and prevents application to unsteady flow simulations involving numerous grid deformation steps. The elastic body analogy method [13] considers the grid as an elastic body and solves the associated set of partial differential equations describing the elasticity problem. Although this method typically produces the best quality meshes, it is also too expensive to be applied to unsteady flow problems such as flapping wings. Recently, several researchers [14–16] have investigated alternative, cheaper methods for mesh deformation based on interpolation schemes. The radial basis function method [14,17] is still

Presented as Paper 6397 at the 26th AIAA Applied Aerodynamics Conference, Honolulu, HI, 18–21 August 2008; received 12 January 2009; revision received 15 July 2009; accepted for publication 21 July 2009.

*Assistant Professor, Department of Mechanical Engineering, 1000 East University Avenue; broget@uwyo.edu. Member AIAA.
†Assistant Professor, Department of Mechanical Engineering, 1000 East University Avenue; jsitaram@uwyo.edu. Member AIAA.
‡Graduate Research Assistant; rharmon2@umd.edu. Member AIAA.
§Graduate Research Assistant; jgrauer@umd.edu. Member AIAA.
¶Langley Distinguished Professor; jhubbar2@umd.edu. Member AIAA.
**Assistant Professor; humbert@umd.edu. Member AIAA.

too computationally expensive to be applied in the present unsteady flow study, but produces grids of very high quality. Liu et al. [15] presented a grid deformation method based on Delaunay graph mapping. Although very fast and efficient, this method does not preserve orthogonality at the surface and can also lead to grid invalidity problems for large grid deformations. Despite these problems, the basic idea in Liu et al. [15] was used in the present study to develop a tailored grid deformation method that could successfully deform a volume grid around very flexible flapping wings. An extension of the method was also developed to improve surface grid orthogonality.

The University of Maryland Transonic Unsteady Navier–Stokes (UMTURNS) code [18] is selected to apply the modifications that are required for inclusion of flexible wings. The UMTURNS code is a compressible Reynolds-averaged Navier–Stokes (RANS) solver that uses body-fitted curvilinear structured grids and has been applied to variety of rotorcraft aeroelastic problems.

The objectives of this work are as follows: 1) implement, test, and validate an efficient grid deformation scheme suitable for modeling large elastic deformations; 2) analyze the experimental measurements of wing motions and aerodynamic loading and decipher their physical significance; 3) combine the grid deformation methodology and the flow solver to obtain an aerodynamic prediction tool; and 4) perform sensitivity studies and correlate analytical predictions with experimental measurements.

II. Methodology

This section is organized into four parts: 1) a brief description of the experiment conducted at the University of Maryland [7], 2) a description of the solution algorithm used in the flow solver, 3) a description of the wing kinematics, and 4) a description of the grid deformation algorithm.

A. Description of the Ornithopter Experiment

At the University of Maryland, researchers have been studying the flight characteristics of ornithopters using modified versions of commercially available radio-controlled models.[††] The ornithopter used in this study was developed and marketed by Kinkade and uses a crank mechanism driven by a rotary motor to flap the wings.[‡‡] The wings of this particular model are flexible structures composed of carbon fiber spars and covered with a rip-stop polyester membrane, with a single wing span of 21 in. and a maximum chord of 11 in.

In collaboration with the Autonomous Vehicle Laboratory at the University of Maryland, a series of shape tracking experiments was conducted on two Morpheus Laboratory ornithopters using a Vicon® vision system (Fig. 1). This system uses six high-speed cameras at 350 frames/s to track the position of 3 mm (about 0.12 in.) reflective markers attached to the wing surface (Fig. 2). The ornithopter frame is rigidly attached to a ground stand, and the wing flapping frequency is controlled by adjusting the power input to the motor. The vertical force (lift) and horizontal force (thrust) produced by the flapping motion are also measured using a 6 deg of freedom strain gauge transducer. More details about the experiment can be found in [19]. Although this experimental setup does not reproduce actual flight conditions, it allows the generation of very accurate measurements of time-varying wing deformations and thus is a valuable tool for validating the present CFD/grid deformation methodology.

B. Flow Solver Algorithm

The CFD code used for the present work is the UMTURNS code [18]. The UMTURNS code is an extensively modified version of the serial TURNS [20] code, which was originally developed by NASA/U.S. Army. The code solves the Reynolds-averaged form of Navier–Stokes equations in both steady and time-accurate formulations on structured curvilinear grids. It also supports the overset-grid capability, which has been shown to be very successful for modeling moving body problems [21]. A finite volume node-centered upwind numerical algorithm is used to discretize the governing equations. In this algorithm, the evaluation of the inviscid fluxes is based on an upwind-biased flux-difference scheme originally developed by Roe [22]. The viscous fluxes are computed using a second-order-accurate finite volume discretization. All the terms in the viscous stress tensor, that is, in all directions, as well as the cross terms are retained in the viscous flux calculations.

The lower-upper symmetric Gauss–Seidel (LU-SGS) scheme developed by Jameson and Yoon [23] is used for the implicit operator. For time-accurate computations, a second-order backward difference in time is used, along with Newton-type subiterations to remove factorization errors and restore formal second-order accuracy. In addition, this code supports deforming mesh computations using the arbitrary Lagrangian Eulerian formulation. Space and time metrics in the case of deforming meshes are computed consistent with geometric conservation law. Two turbulence models, the Baldwin–Lomax [24] model and Spalart–Allmaras [25] one-equation model, are available for achieving RANS closure. The UMTURNS code has been used extensively for rotorcraft aeroelastic computations and has a good validation base [26]. For rotorcraft problems, blade deformations are quite benign compared with the extremely large deformations seen in the present study, and a simple interpolation method was enough to deform the grids around the helicopter blades [27].

Fig. 1 Vicon® camera system used for the measurement of wing motion.

Fig. 2 Marker locations on the ornithopter wing.

[††]Data available online at http://www.morpheus.umd.edu [retrieved 9 September 2009].

[‡‡]Data available online at http://www.ornithopter.org/store/kinkade.gear.html [retrieved 9 September 2009].

Table 1 Flow characteristics at seven flapping frequencies extracted from the ornithopter test

Frequency, Hz	Maximum Reynolds number	Maximum Mach number
3.24	105,000	0.0262
3.85	125,000	0.0314
4.23	140,000	0.0350
4.65	157,000	0.0393
5.01	173,000	0.0432
5.41	190,000	0.0474
6.09	213,000	0.0533

The dissipation terms in the inviscid fluxes computed by Roe's [22] approximate Riemann solver become unbounded at very low Mach numbers, leading to large truncation errors. Additionally, the convergence of the numerical scheme degrades because of the large disparity between the material and the acoustic wave speeds. Therefore, in this work, the Turkel-type [28] low Mach preconditioning is applied to the Roe scheme. Turkel-type low Mach preconditioning enhances convergence by modifying the acoustic wave speeds (bringing them closer to the material wave speed) and also scales the dissipation terms such that they are bounded at low Mach numbers. The details of the implementation of the Roe–Turkel Riemann solver can be found in Gupta [29], who implemented the preconditioning in the UMTURNS code to study very low Mach number flows around helicopter fuselages.

Preconditioned dual time procedures [30] are deemed necessary for ensuring good residual convergence for time-accurate flow computations with large time steps. The UMTURNS code does have an implementation of the preconditioned dual time procedure [31] using the Pullium–Chausse implicit operator [32]. Unfortunately, this scheme was found to be not robust enough for the large mesh deformations. Therefore, the baseline LU-SGS scheme with Newton-type subiterations is retained as the implicit operator. Small time steps (at least 2880/cycle) were found to be required to obtain the necessary residual convergence (two orders) in the subiteration level.

No-slip boundary conditions are enforced at the wall boundaries. A perfect adiabatic wall is assumed and the normal momentum equations are solved to compute the surface pressure. Characteristic-type boundary conditions using Riemann invariants are used for the outer boundaries. For applications with low Mach preconditioning, the outer boundary conditions are modified to be consistent with the wave speeds of the preconditioned system.

No attempt is made to model laminar/turbulence transition, and all studies are conducted using a fully turbulent flow assumption. The algebraic Baldwin–Lomax turbulence model is used for RANS closure.

C. Wing Motion Analysis

The test this study focuses on lasts about 20 s, during which the throttle was first increased steadily to its maximum setting and then decreased in a stepped manner, to allow data acquisition of both motion and forces at about seven steady frequencies. Table 1 shows the value of frequency, maximum Reynolds number, and maximum Mach number for these seven frequencies. The frequency varies from about 6 Hz down to 3 Hz, corresponding to a maximum Reynolds number of 213,000 (computed based on local chord and velocity) and a maximum tip Mach number of 0.05.

Figure 3 illustrates the range of motion encountered during the test. Figure 3a shows how the various wing angles (flap, lag, and twist) vary with increasing flapping frequency. The flap and lag angles are defined based on the local orientation of the leading-edge spar, whereas the tip twist angle is defined based on the orientation of the tip chord section. The root flap angle is nearly independent from the frequency, with a steady value of around 25 deg half peak to peak. This is expected because this angle is imposed by the crank

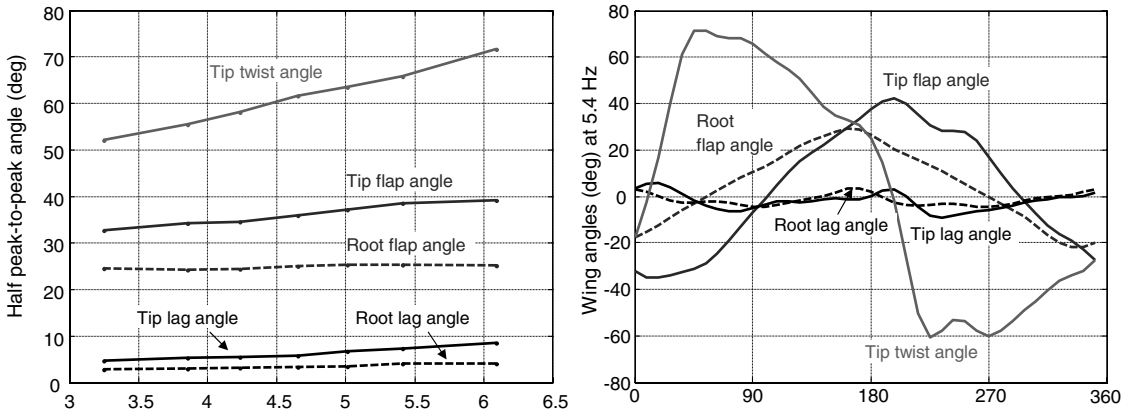

a) Flapping frequency (Hz) **b) Angular position in cycle (deg)**

Fig. 3 Variation of different wing angles: a) flapping frequency, and b) angular position in one flapping cycle.

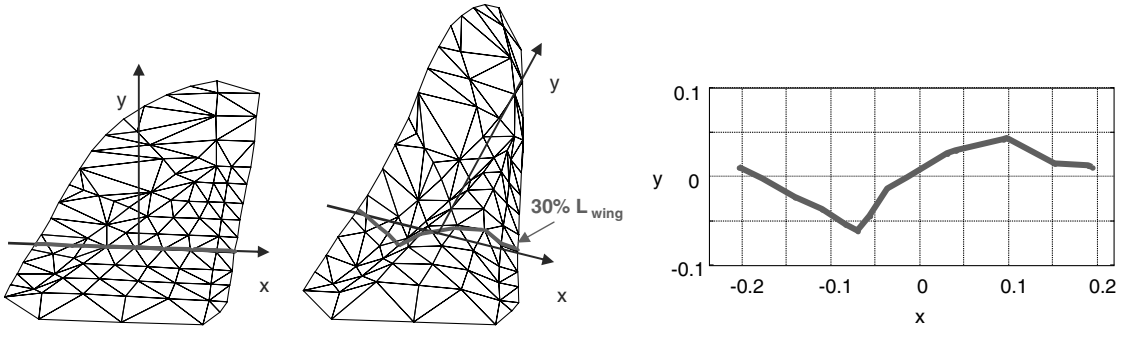

a) Undeformed wing **b) Deformed wing** **c) Deformed chord at 30 % L_{wing}**

Fig. 4 Example of chord deformation.

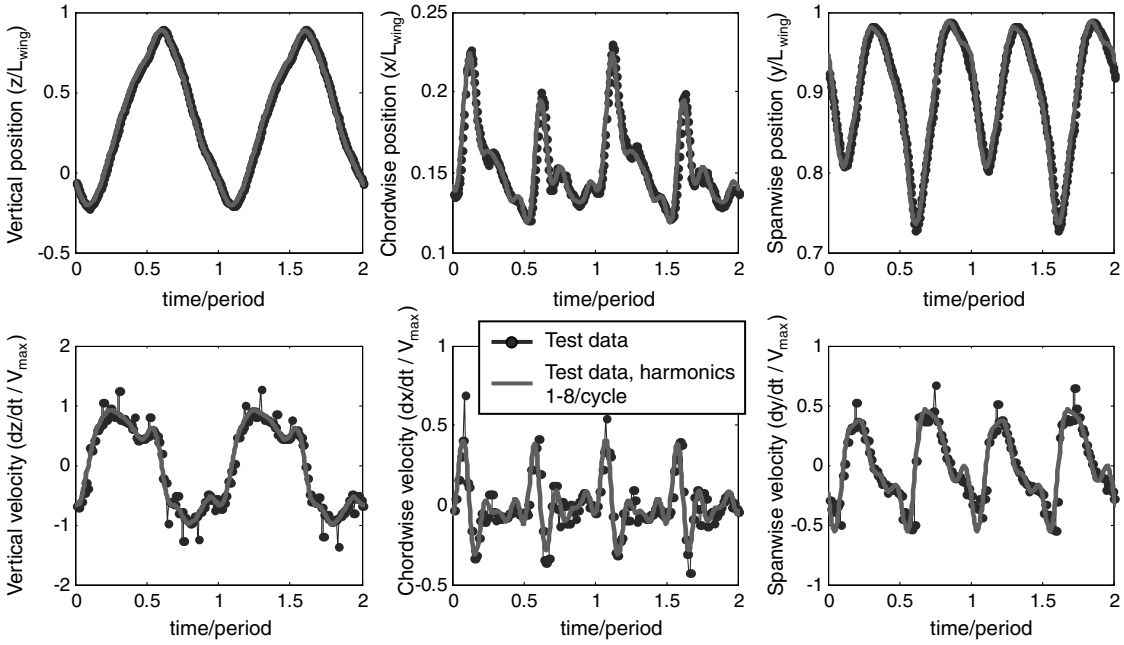

Fig. 5 Comparison of marker position and velocity between original test data and filtered test data at 5.4 Hz flapping frequency for the marker point corresponding to the largest difference.

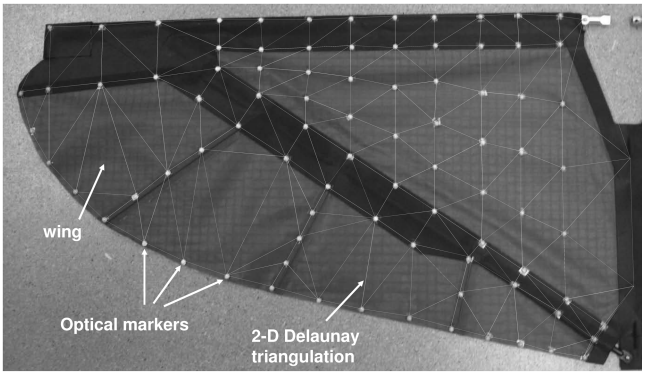

Fig. 6 Two-dimensional Delaunay triangulation of wing markers.

mechanism, which induces wing flapping. The tip flap angle includes wing flexibility and increases from about ± 32 deg at 3.2 Hz to almost ± 40 deg at 6 Hz. The lag angle, although not negligible, remains much smaller, less than ± 10 deg for the entire frequency range. The tip twist angle is very large, increasing almost linearly with frequency from around ± 50 deg to more than ± 70 deg at 6 Hz. Figure 3b shows the details of the angle variation in one flapping cycle for a particular frequency during the test (5.4 Hz). The root flap angle waveform is almost triangular in shape, with a large dominant 1/cycle frequency component. Other wing angles such as tip flap and twist also vary dominantly at a frequency of once per cycle, but do include significant higher harmonic content as well.

Apart from very large twist, flap, and lag deformations, the high wing flexibility also induces important camber deformation in the chordwise direction. This is shown in Fig. 4, which illustrates the wing before and after deformation at a selected time instance corresponding to the largest chord deformation. Figure 4c shows the deformed chord at 30% of the wing length in the deformed frame. A sharp angle of almost 90 deg is apparent (corresponding to the diagonal spar location), which is caused by the difference in flexibility between different parts of the wing.

D. Grid Generation and Deformation

The CFD solver requires a structured curvilinear grid encompassing the moving wings. At each simulated time step, this grid must be adapted to conform to the current wing shape. The need to perform this operation at each time step precludes the use of time-expensive elasticity-based deformation methods. In addition, because of the drastic deformations undergone by the wings, existing grid deformation methods based on the spring analogy, although less expensive, are also ill suited. As a result, a specific method was developed to efficiently generate and deform a grid around a pair of flapping wings.

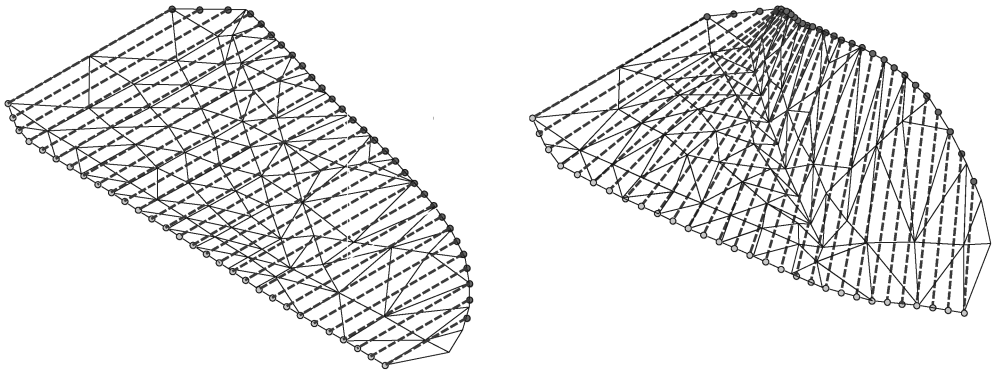

a) Undeformed wing **b) Deformed wing**

Fig. 7 Segments defining location of 2-D spanwise grid planes, before and after deformation.

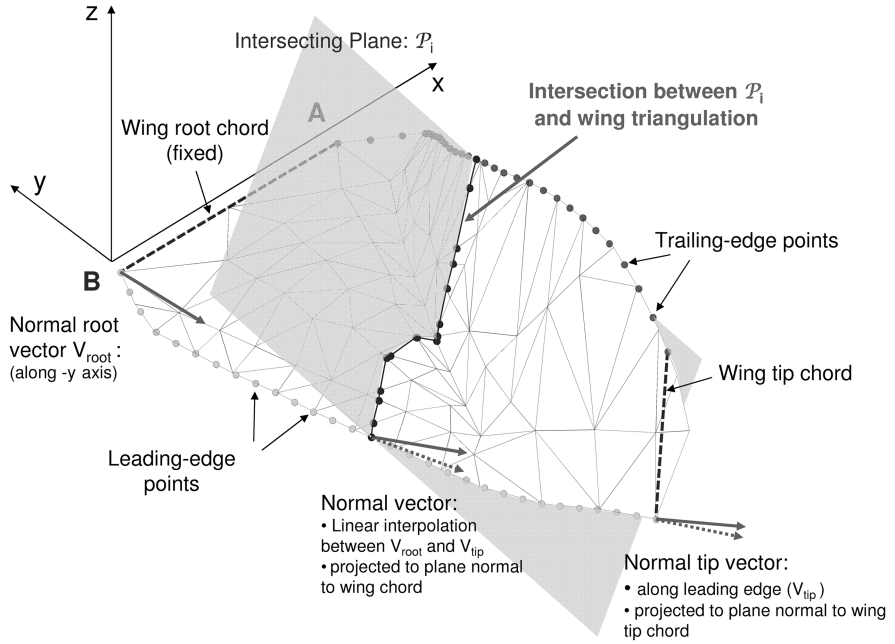

Fig. 8 Method to define planes of each 2-D grid along the wing span.

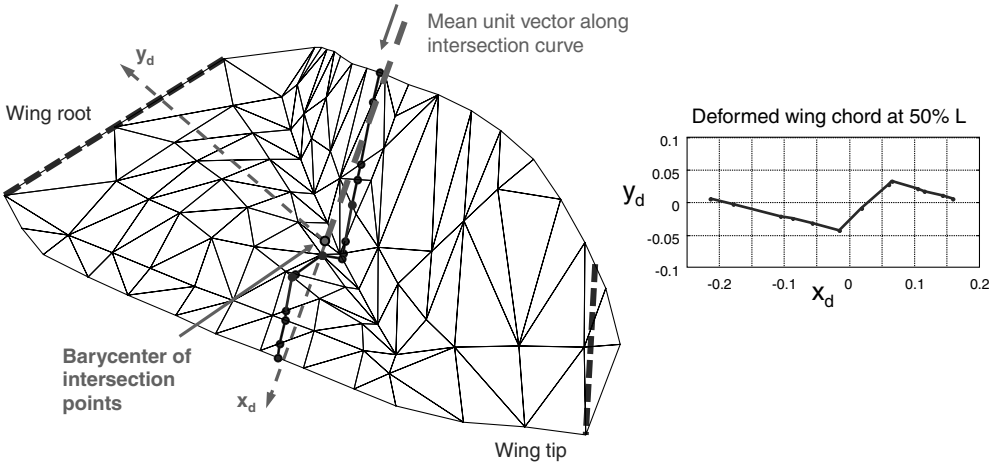

Fig. 9 Definition of the deformed axes.

The position data from the Vicon® system are available at 90 sensor points on the wing and four points on the tail. For CFD simulation, the tail is not modeled and only the pair of wings is considered. To minimize the effects of measurement noise, the coordinates of each sensor point on the wing are first filtered by retaining the first eight harmonics (integer multiples of the basic flapping frequency). This filtering step results in a mean position error of about 0.5% of the wing length (about 0.1 in.). A comparison of unfiltered and filtered positions and velocities is presented in Fig. 5 for a point located on the wing trailing edge and close to the wing tip, which corresponds to the worst-case position difference. For each time step of the flapping cycle, the filtered position data are then used to construct a three-dimensional curvilinear structured grid to be used by the CFD solver. This grid is constructed by concatenating a series of two-dimensional deformed grids along the wing and processing the grid at the wing extremity separately. The two sensor points located along the wing centerline are assumed to remain stationary. The entire grid is completed by reflecting the grid about the plane of symmetry defined by this centerline and the vertical axis.

In more detail, the grid construction procedure is as follows:

1) First, the two-dimensional Delaunay triangulation of the sensor points is constructed using the undeformed, two-dimensional wing configuration (Fig. 6).

2) To identify the location of grid planes along the wing span, a number of points are equally distributed along the wing leading edge and connected to corresponding points along the trailing edge (with the same y coordinate). It is assumed that the wing points along the segment from each leading-edge point to the corresponding trailing-edge point remain coplanar when the wing deforms. This is illustrated in Fig. 7, which shows these segments for the undeformed and deformed wing configuration.

3) For each spanwise segment, a plane is defined that passes through the local leading- and trailing-edge points in the following way:

a) For the leading-edge point most outboard of the wing, this plane is normal to the wing surface at the tip.

b) For the leading-edge point most inboard of the wing (passing through the centerline), this plane is the plane formed by the centerline and the vertical axis.

c) For other leading-edge points along the wing, the plane of the grid is formed by applying a uniform rotation between the tip plane and the root plane (about the axis formed by the intersection of the tip and root planes). This is illustrated in Fig. 8.

4) For each plane along the wing, the curve formed by the intersection of the plane and the wing surface is identified. The deformed body axes are computed using the average unit vector

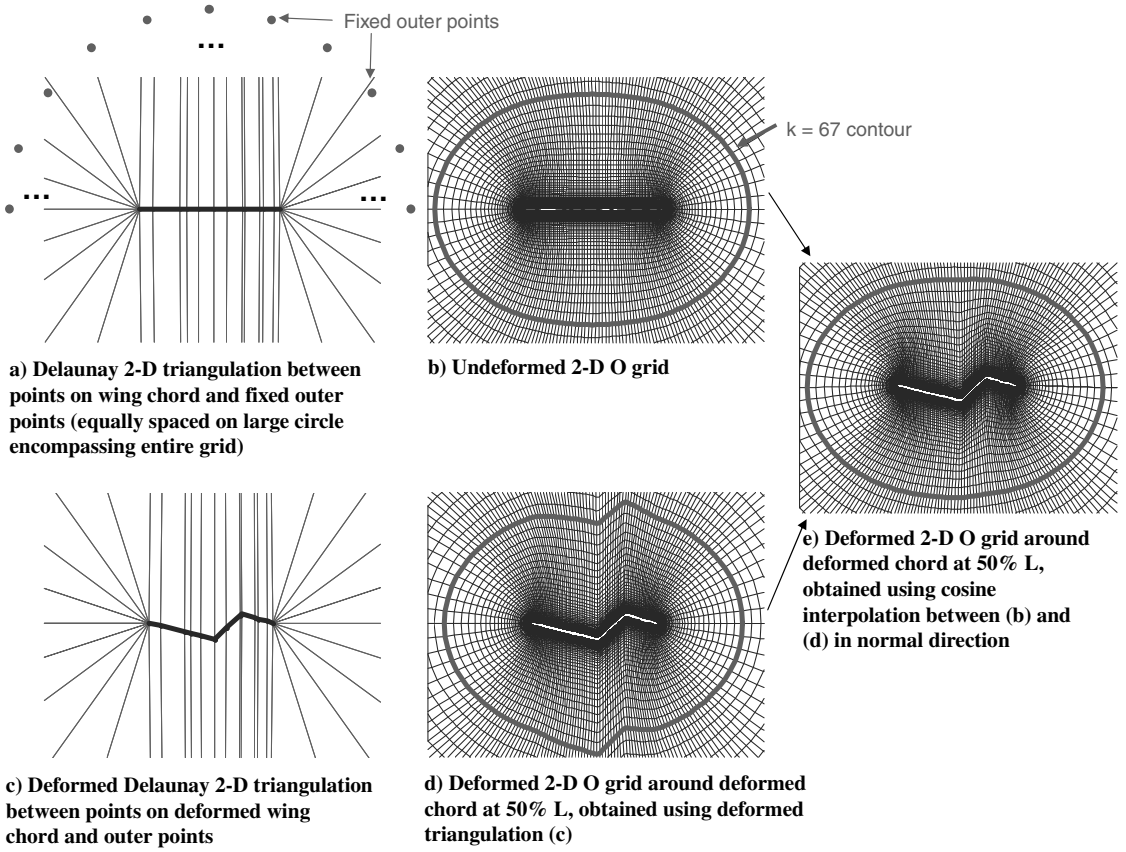

Fig. 10 Deformation method for 2-D grids.

along the intersecting curve (pointing toward the wing leading edge). This is illustrated in Fig. 9.

5) In the deformed axes, an undeformed two-dimensional grid (of *O*-grid topology) is created around the equivalent undeformed wing section. Using the Delaunay graph method [15], this grid is then deformed to conform to the actual wing section. The grid obtained is then smoothed by using a cosine interpolation in the normal direction between the deformed and undeformed configurations. Noting the undeformed grid G_u and the deformed grid G_d, the final deformed grid G is computed as follows:

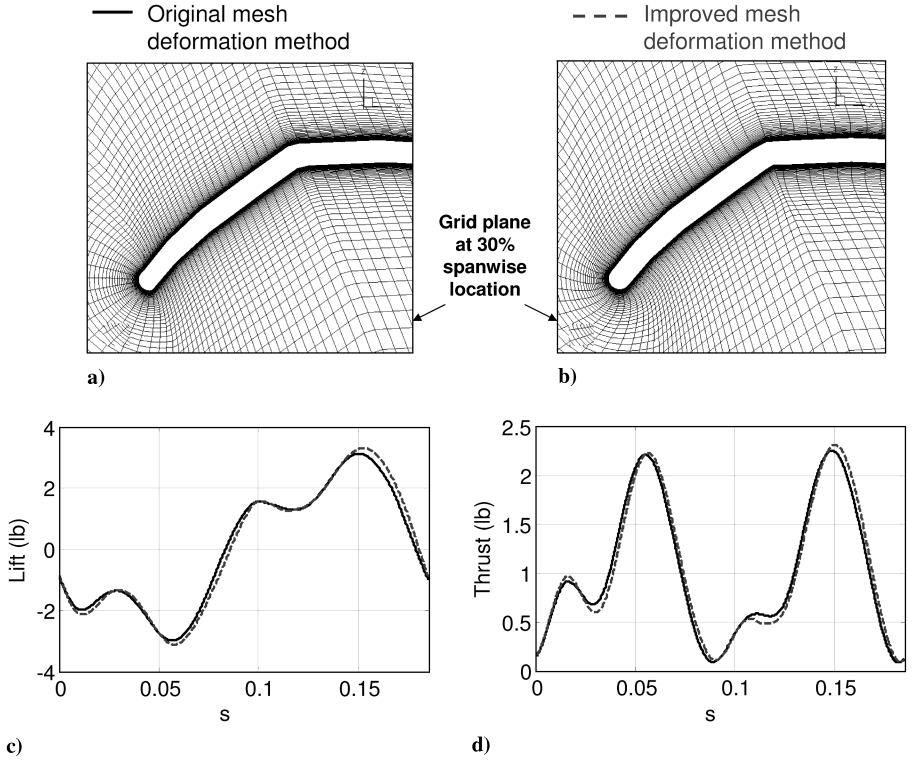

Fig. 11 Effect of grid surface orthogonality on CFD-predicted lift and thrust (5.4 Hz flapping frequency).

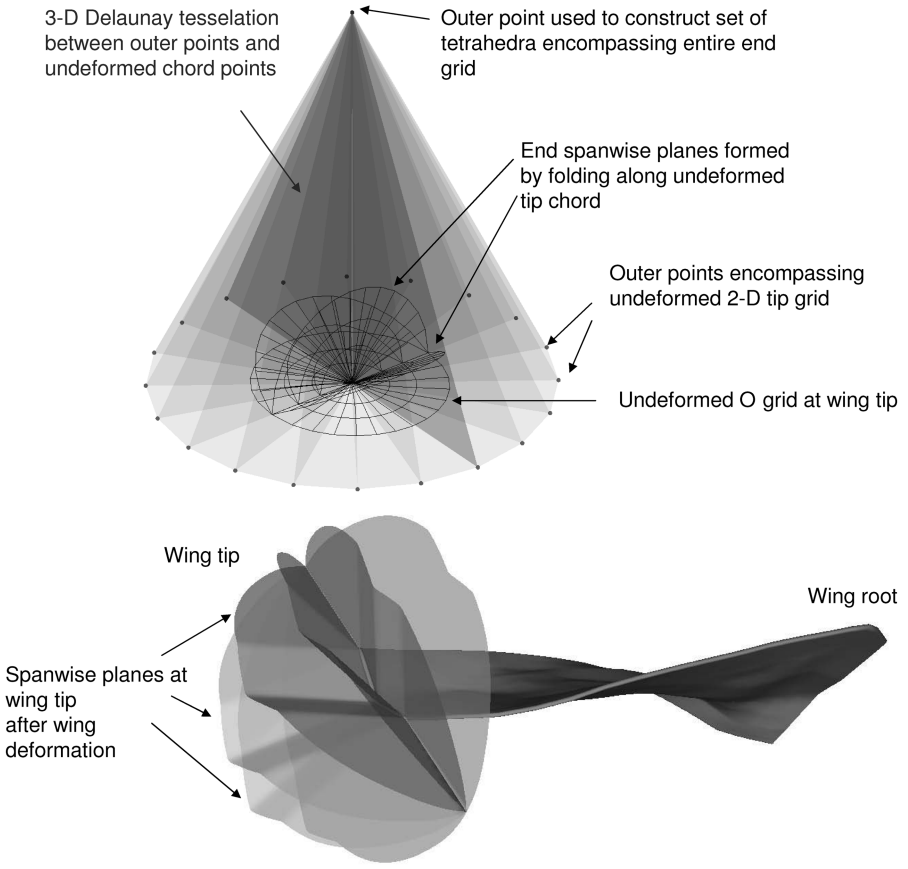

Fig. 12 Grid generation and deformation at wing extremity.

$$G(j,k) = \mu G_d(j,k) + (1-\mu)G_u(j,k), \quad \text{with}$$
$$\mu = \tfrac{1}{2}\{\cos[(k-k_i/k_f-k_i)\pi]+1\} \tag{1}$$

where j is the wraparound direction, k is the normal direction, and k_i and k_f are the initial and final indices in the normal direction between which the interpolation is applied. This step is illustrated in Fig. 10.

This method is very efficient but does not maintain grid orthogonality at the wing section, which can lead to increased numerical errors for viscous flow simulations. To investigate the effects of this problem on simulation results, the Delaunay graph method was modified to improve grid orthogonality at the surface. The basic idea remains identical to that of the Delaunay graph method, namely, to deform only a geometric construction around the domain to be deformed and use interpolation to compute the deformed positions in the entire domain. However, instead of using a triangle-based tesselation of the domain as in the Delaunay graph method, the modified method uses a tesselation made of quadrilaterals.

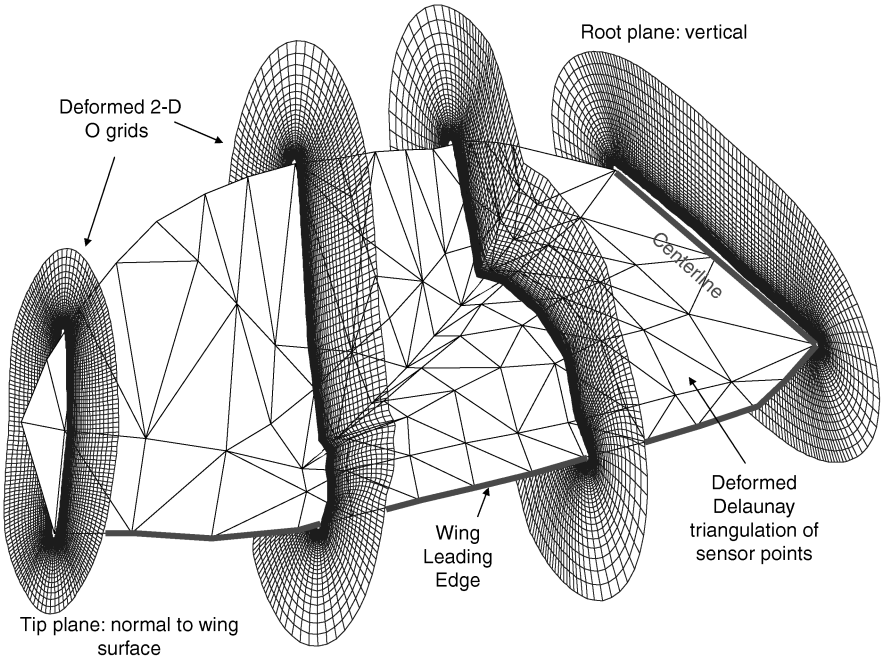

Fig. 13 Deformed 2-D grids along the wing span before interpolation in normal direction.

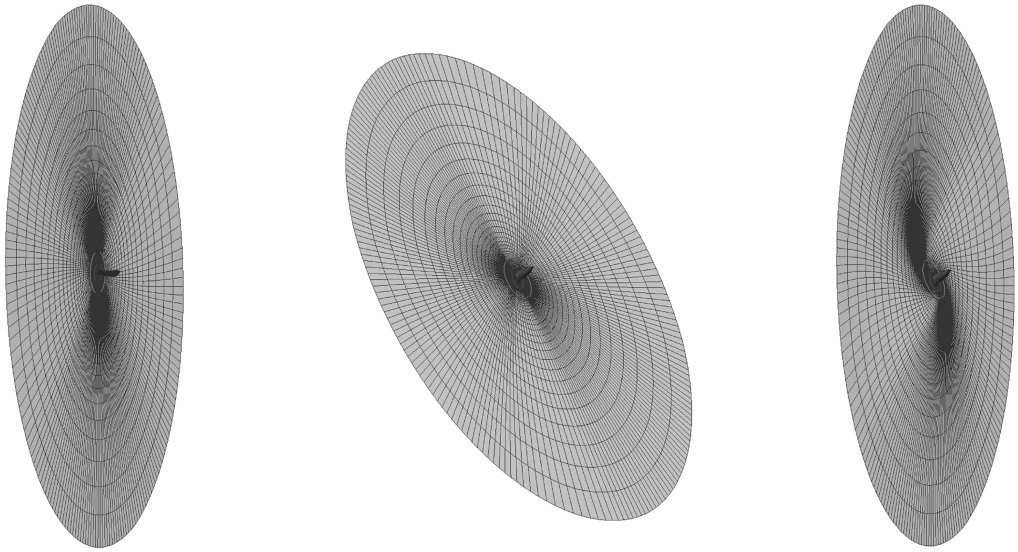

a) Undeformed wing and grid

b) Deformed wing and grid

c) deformed wing and grid with cosine interpolation from (a) to (b) in normal direction

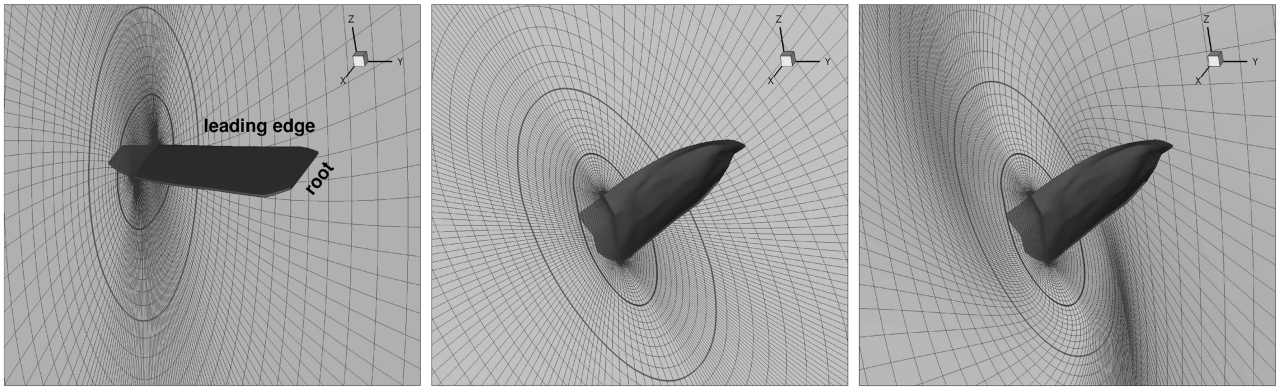

Fig. 14 Interpolation between deformed and undeformed 3-D grids in normal direction.

A geometric method is devised to deform the quadrilateral tesselation, and the deformed grid is computed by interpolation, assuming that each grid point maintains its relative position within the encompassing cell. The quadrilaterals adjacent to the wing section have the smallest normal extent so that, after deformation, orthogonality to the section is mostly conserved.

Figures 11a and 11b show the deformed grid at a wing section located at 30% wing span from the root using the original method and the modified method. Figures 11c and 11d show the lift and thrust variation predicted by the CFD solver using both types of grids. Even though the grid orthogonality at the wing surface is significantly improved in the modified method, the results change only marginally. Therefore, the original grid deformation scheme, which is simpler and more efficient, is used in the present study.

6) The extremity of the grid is closed by considering the plane most outboard of the wing and folding it along the line corresponding to

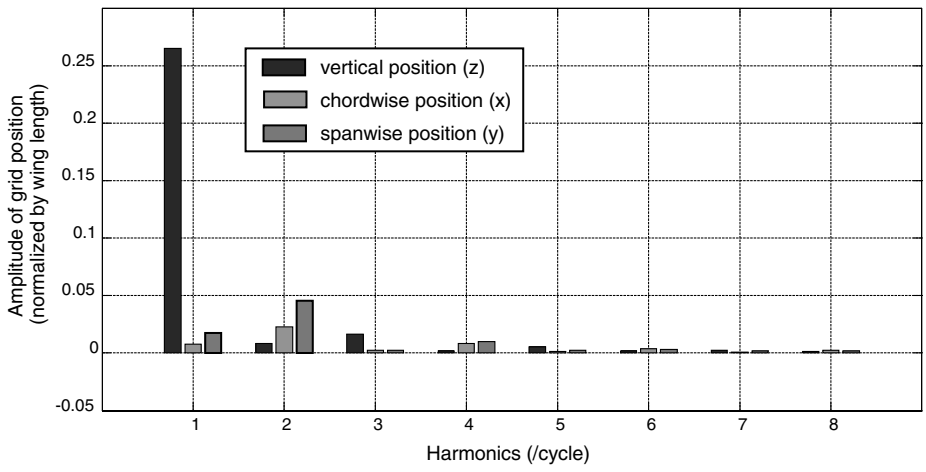

Fig. 15 Harmonic content of grid coordinates averaged over the wing surface (frequency = 5.4 Hz).

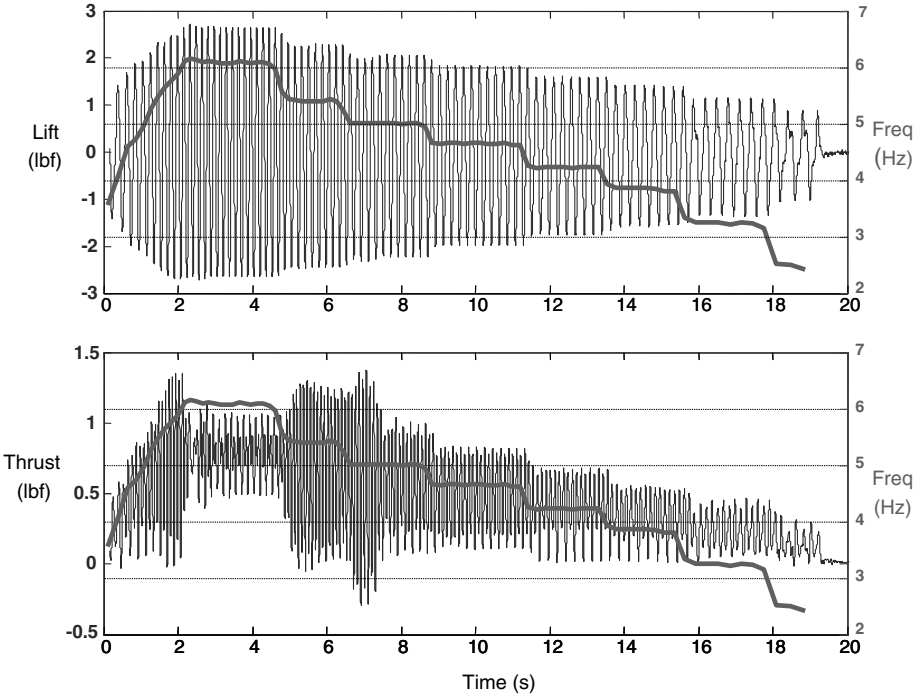

Fig. 16 Lift and thrust variation during entire test.

the equivalent undeformed tip chord until the two half-planes meet. This series of planes is then deformed to conform to the actual deformed tip chord by applying the Delaunay graph method in three dimensions, as shown in Fig. 12.

7) The planes along the wing span extend in the normal direction for a distance of about 20 times the maximum wing chord. Because of the large wing flapping deformation, these planes intersect each other for large k values (direction normal to the wing surface). This situation is illustrated in Fig. 13. To remedy this, a cosine interpolation similar to that described in Eq. (1) is applied between the deformed (invalid) three-dimensional grid and the undeformed grid around the undeformed, flat-wing configuration. This step is illustrated in Fig. 14. Figure 14a shows the undeformed, flat wing and a grid section at about 75% wing span. The top figure shows a view of the entire grid, whereas the bottom figure shows a close-up of the grid closer to the wing. Figure 14b shows the deformed wing and grid section. It can be seen that, because of the large normal extent of the grid and the large wing deformation in the spanwise direction, grid sections would intersect each other. Figure 14c shows the results of interpolation between the deformed and undeformed grids in the normal direction. After this step, the final grid is valid with no intersection between adjacent planes along the span.

8) Finally, the entire volume grid is completed by reflecting it about the plane of symmetry defined by the centerline and the vertical axis. This center plane is assumed to remain constant (no rotation) through the flapping cycle.

To reduce computational cost, the deformed grid is computed for a full flapping cycle at a small number of time steps (40). The first two harmonics for each grid point coordinate are then extracted and used in the flow solver to interpolate the grid position at any time during

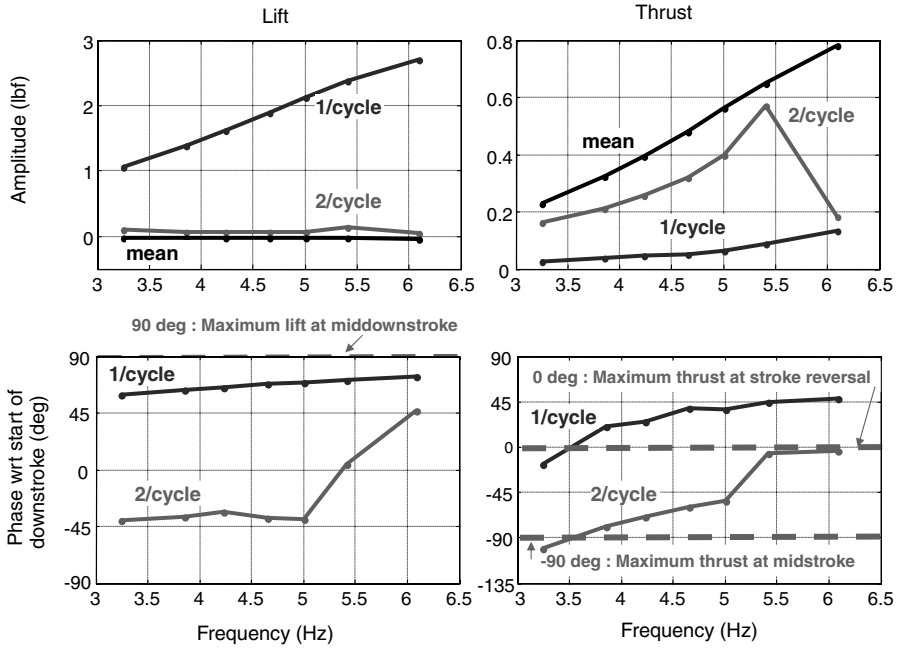

Fig. 17 Harmonic analysis of measured lift and thrust.

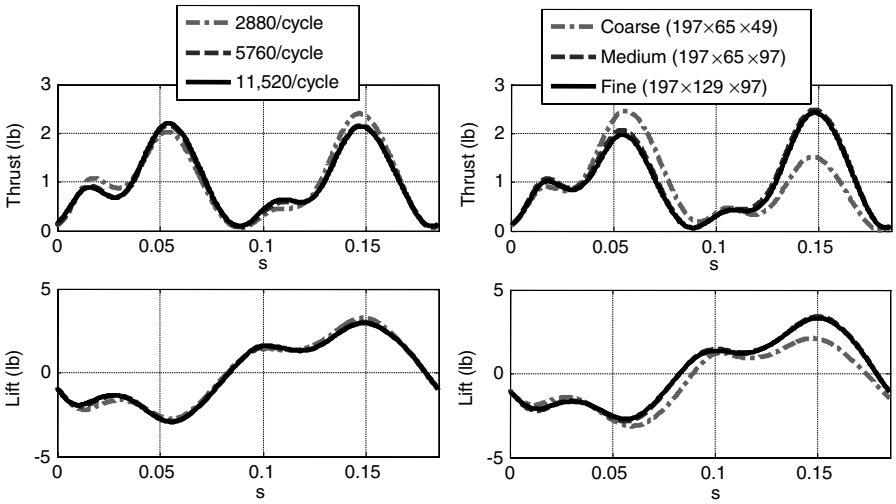

a) Time step sensitivity (with medium grid)

b) Grid dimension sensitivity (with 2880 points per cycle)

Fig. 18 Results sensitivity to simulation parameters.

the flapping cycle. Figure 15 shows the first eight harmonics of the grid position in the vertical, chordwise, and spanwise directions averaged over the wing surface. It can be seen that the first two harmonics are largely dominant and that including more deformation harmonics does not significantly change the prediction of the 1/cycle and 2/cycle loading. However, it does introduce higher harmonic content in the predicted loading.

III. Results

A. Analysis of Experimental Data

Both lift and thrust were measured using a 6 deg of freedom strain gauge transducer during the ornithopter experiment. Lift refers to the force in the vertical direction, whereas thrust refers to the force in the horizontal (forward flight) direction. Figure 16 shows the variation of lift and thrust with time for the entire duration of the test (about 20 s). To better identify the different phases of the test, the variation of the flapping frequency is superimposed on this figure, with the corresponding axis shown on the right-hand side. The flapping frequency is first steadily increased to its maximum value of about 6.1 Hz, after which it is progressively decreased in steps down to its minimum value of about 2.5 Hz. Seven stages are identified during which a quasi-steady throttle level is achieved with a flapping frequency from 6.1 to 3.2 Hz. The lift amplitude increases steadily with increasing flapping frequency, whereas the thrust amplitude shows a peak in amplitude between 5 and 5.5 Hz. At higher frequencies (6.1 Hz), the thrust amplitude shows a sudden drop. Figure 17 shows a harmonics analysis of the lift and thrust data. Only the mean value and the first two dominant harmonics are shown. The mean value of the lift is negligible, whereas the mean value of the thrust is larger than the vibratory components and increases linearly with flapping frequency. As expected, the lift varies mostly at a frequency of once per flapping cycle (1/cycle), whereas the thrust varies mostly at a frequency of twice per flapping cycle (2/cycle). The variation with frequency of both amplitude and phase are shown for both harmonics. The phase is defined with respect to start of the downstroke, which is identified by the considering the mean flapping angle along the wing leading edge. This is because, at the middownstroke, the wing plunge velocity reaches its maximum, and the mean angle of attack is positive for most spanwise sections. Because plunge velocity and local angle of attack are the main factors in determining lift, it is expected that the lift will have a maximum positive value around the middle of the downstroke, which corresponds to a phase of 90 deg (other factors such as unsteady effects and inertial forces also contribute to the exact timing of the maximum lift). Test data shows that the maximum occurs at a slightly different phase angle, varying from about 60 deg at 3.5 Hz to 75 deg at 6 Hz. It is also expected that the thrust will have a maximum positive value around the middle of both the downstroke and the upstroke, that is, twice per flapping cycle. This would correspond to a phase of ± 90 deg. However, the test data show that the phase of the 2/cycle thrust changes drastically during the test, from -90 deg at low frequencies (3.5 Hz) to 0 deg at higher frequencies (6 Hz). A phase of 0 deg means that maximum thrust occurs at each stroke reversal, which is somewhat counterintuitive. Inertial forces also contribute to the measured thrust, and these do reach a maximum at stroke reversal. However, as will be shown later (Fig. 23), inertial forces are significantly smaller than aerodynamic forces and are not sufficient to explain the 0 deg phase of maximum thrust. A sudden change in thrust phase occurs when the flapping frequency is between 5 and 5.5 Hz, which also corresponds to the peak in thrust amplitude. The peak in variation of amplitude and the associated phase reversal are typical of a damped harmonic system that operates near resonance. Therefore, it can be deduced that the entire system (composed of a vehicle with wings and support mounts) shows resonance of an in-plane mode at the frequency of the aerodynamic thrust variation (i.e., twice the flapping frequency at 10–11 Hz). In addition, the thrust variation also shows a 1/cycle variation, indicating the asymmetry in thrust generation between the up and down strokes.

B. Sensitivity Studies

Before attempting correlation of test data with CFD simulated results, the sensitivity of the CFD results to variation in the simulation parameters needs to be ascertained. A limited sensitivity study is performed based on grid spacing and time step size, and the results are presented in Fig. 18. Figures 18a and 18b show the changes in predicted lift and thrust with time step size and grid dimensions, respectively. A time step reduction from 2880 to 5760 points per cycle (corresponding to a reduction in angular step size from 0.125 to 0.0625 deg) results in a maximum change of about 11% in thrust, whereas a further reduction to 11,520 points per cycle (0.03125 deg) only changes the thrust by at most 2.5% over the flapping cycle, which is within the margins of the test data tolerance. As a result, a time step of 5760 points per cycle was determined to be adequate for the baseline simulations. The lift simulation results appear less sensitive than the thrust to changes in time step size.

Table 2 Grid dimensions (number of grid points)

	Wraparound	Spanwise	Normal	Total
Fine	197	129	97	2.47×10^6
Medium	197	65	97	1.24×10^6
Coarse	197	65	49	0.63×10^6

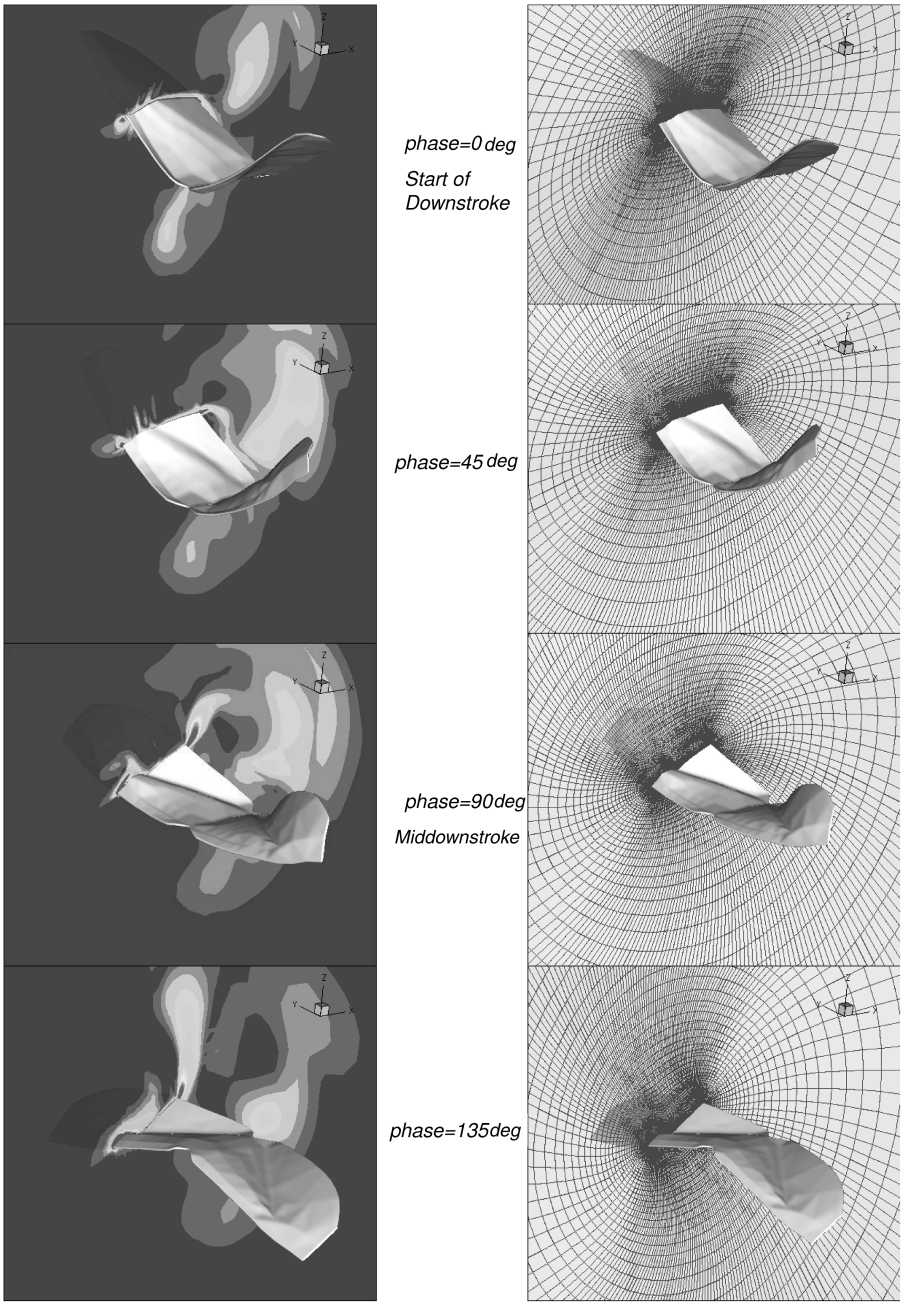

Fig. 19 Vorticity contours (left) and deformed grid (right) at 50% span location during downstroke of the wing (frequency = 5.4 Hz).

Three grid dimensions were tested: a coarse grid containing about 2.5×10^6 points, a medium grid with about 1.25×10^6 points, and a coarse grid with about 0.6×10^6 points. Details of the grid dimensions are shown in Table 2. Thrust simulation results change by about 35% when refining the grid from coarse to medium and by about 4% with a further refinement to the fine grid. Therefore, the medium grid was adopted as sufficient for the CFD analysis.

C. Qualitative Analysis of CFD Results

Visualizations of the ornithopter flowfield are presented to provide qualitative information of the physics involved. Figures 19 and 20 show snapshots of the flowfield during one full cycle of the wing motion. The sequence starts from the time instance at which the wing is in the maximum upward displacement position, that is, just before the beginning of the down stroke. The separation zones produced by the previous upward motion of the wing are clearly visible in isovorticity contours at this location. During the downstroke, the wing moves through this separation zone, producing increased lift and thrust. At the end of the downstroke, the separation zones below the wing have disappeared and the flow is beginning to separate above the wing. As the wing reverses and progresses on the upstroke, large separation zones start forming again below the wing. It can be observed that, because of the specific wing kinematics (combination of flapping and torsion), the separation produced on the upstroke and downstroke is asymmetric, that is, there is a larger amount of separation on the lower side of the wing compared with the upper side. Also, the vortices created by the wing are pushed backward, indicating the net horizontal momentum created by the wing motion, which results in thrust production. The corresponding deformed grids are also shown on the right-hand side of each flow visualization image, to illustrate the quality of the grid deformation scheme. Figures 21 and 22 show in more detail the deformed grid during the flapping cycle. Figure 21 shows the grid surface located at 50% of the wing span (constant spanwise grid coordinate), whereas Fig. 22 shows the grid surface located at 50% of the wing chord (constant wraparound grid coordinate).

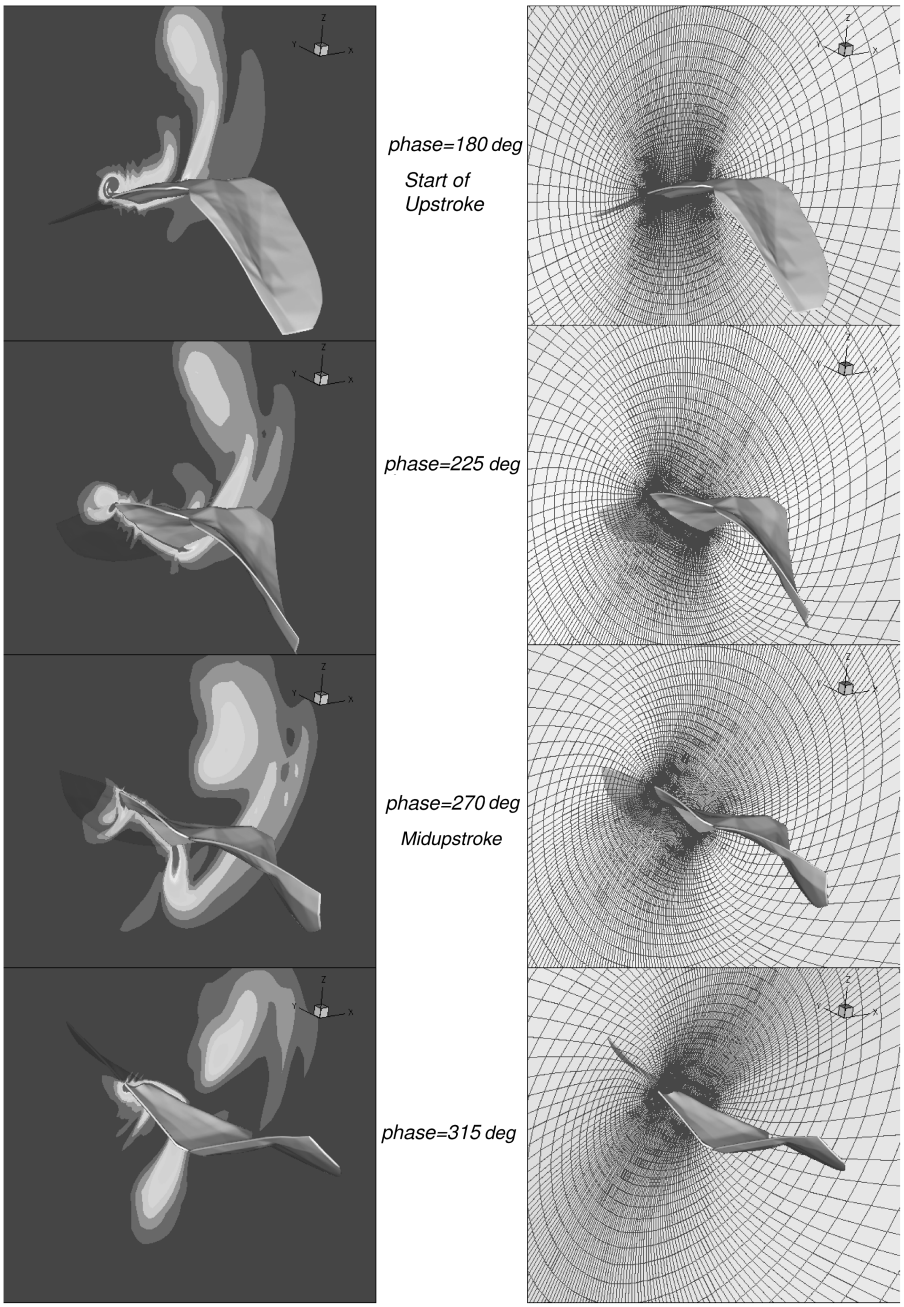

Fig. 20 Vorticity contours (left) and deformed grid (right) at 50% span location during upstroke of the wing (frequency = 5.4 Hz).

D. Correlation of CFD Results with Test Data

The results are first analyzed in detail for a particular time slice during the test, corresponding to a frequency of 3.2 Hz. The results are then presented for the entire frequency range. These results are obtained using a medium-size grid, a time step of 0.0625 deg (5760 points per cycle), and a wing thickness of 2.5% of the maximum chord.

Figure 23 shows the variation of lift and thrust with time over one flapping cycle, comparing the test data with CFD results. The CFD analysis only simulates the aerodynamic force on the wing, whereas the load cell sensor measurement also captures the contribution from the inertial forces in the system due to wing accelerations. Therefore, the analytical results including the estimated inertial forces are also shown with dashed lines in the figure. The computation of inertial forces is based on the estimated wing mass distribution (shown in Fig. 24) and the second derivatives of the measured wing positions. Because the latter are affected by measurement noise, there is some amount of uncertainty in the computed inertial forces. Wing accelerations are computed based on the position harmonics and, to reduce the effect of measurement noise, only the first two harmonics are considered (1 and 2/cycle). Another possible source of error comes from the fact that, besides the flapping wings, electronic components such as the motor and battery are also located above the force sensor. Because of their relatively large weight, these components can contribute significantly to inertial forces, especially during resonance. Figure 23 shows that, for this particular frequency (3.2 Hz), the analysis accurately captures both the phasing and the amplitude of the lift variation during the flapping cycle. The phasing of the 2/cycle thrust, as well as the mean thrust, are also well predicted (within 5%). However, the 2/rev thrust amplitude is overpredicted by about 10%. Including the estimated inertial forces in the analysis slightly improves the thrust correlation; however, this effect remains quite small.

Figure 25 presents the same correlation results in a different format, plotting the lift and thrust versus the mean flapping angle along the wing leading edge. The CFD analysis predicts that the maximum lift occurs at just about the middle of the downstroke, whereas the test data show that the maximum lift occurs earlier, at

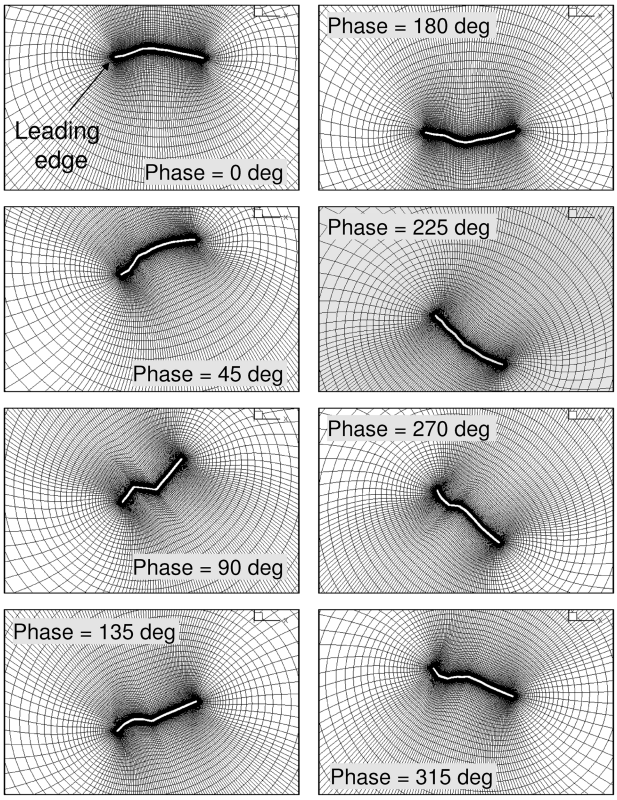

Fig. 21 Variation of the grid surface at 50% wing span during one flapping cycle (frequency = 5.4 Hz).

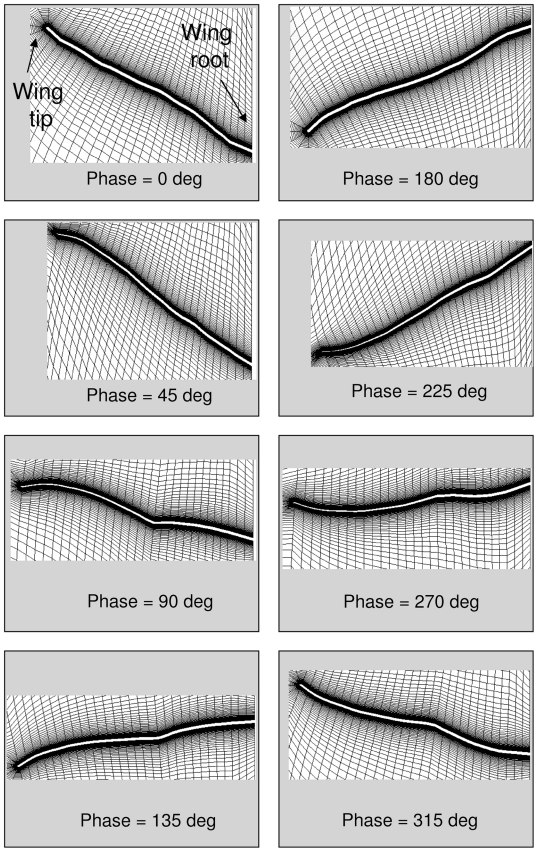

Fig. 22 Variation of the grid surface at 50% wing chord during one flapping cycle (frequency = 5.4 Hz).

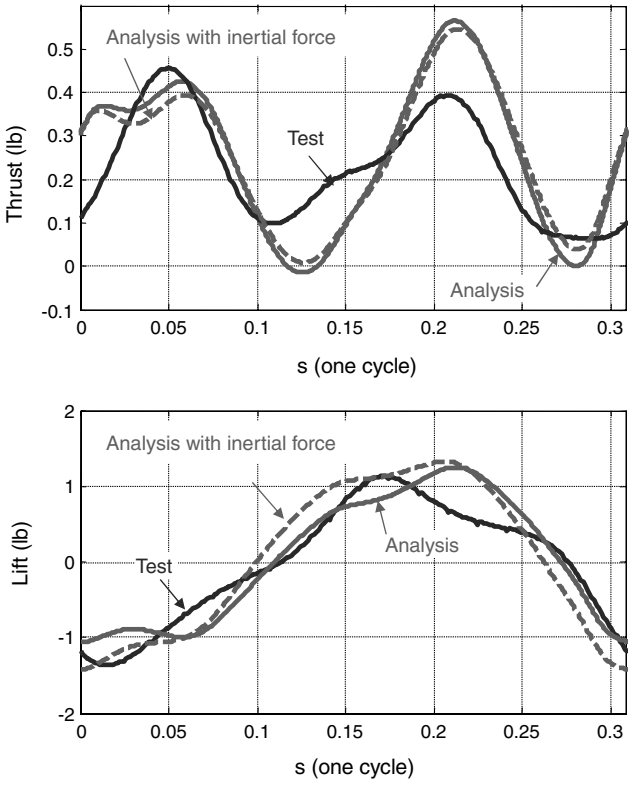

Fig. 23 Lift and thrust variation with time at 3.2 Hz flapping frequency compared with test data.

about a quarter of the downstroke. Including the estimate of the inertial forces moves the phasing of the maximum lift slightly toward the test results. For the thrust force, both the analysis and experiment show that the maximum thrust occurs twice per cycle, at around each midstroke. However, the analysis predicts significantly larger thrust at the middle of the downstroke compared with the middle of the upstroke, whereas the test data show a larger thrust during the upstroke.

Figure 26 presents the lift and thrust correlation results for the entire frequency range tested during the experiment, from 3 to 6 Hz. Only the dominant force harmonics are considered, once per cycle for the lift and twice per cycle for the thrust, and their amplitude and phase with respect to the start of the downstroke are plotted versus the flapping cycle frequency. Both the test and analysis show that the lift amplitude varies almost linearly with frequency, from about 1 lb at 3 Hz to about 3 lb at 6 Hz. The CFD analysis by itself slightly overpredicts the amplitude of the 1/cycle lift by about 8%; however,

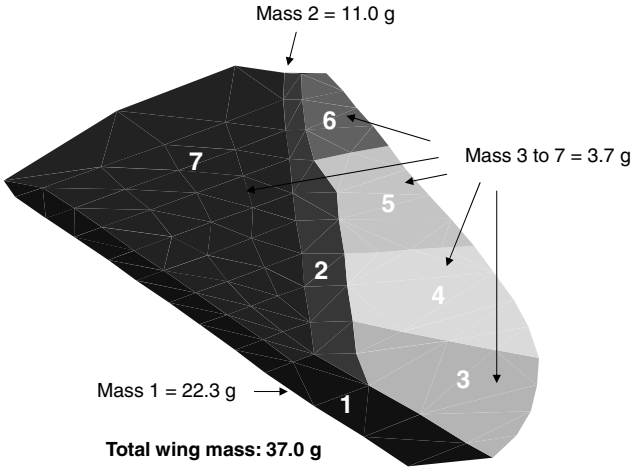

Fig. 24 Estimated wing weight distribution.

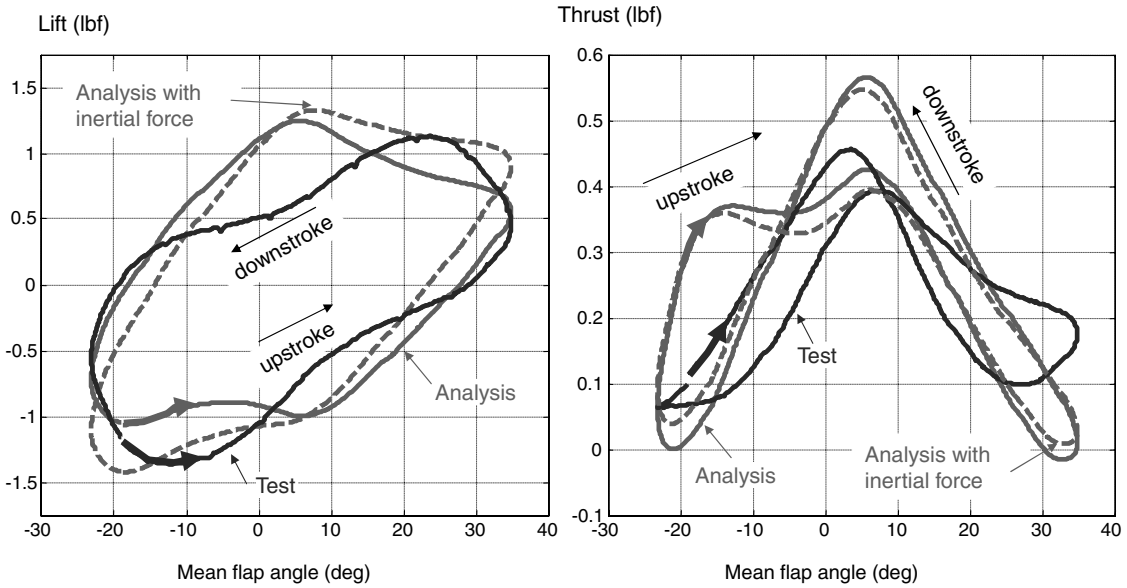

Fig. 25 Lift and thrust variation with flapping angle at 3.2 Hz flapping frequency compared with test data.

including inertial effects deteriorates the correlation with the test data. Both the test and analysis also show that the lift phasing with respect to the start of the downstroke remains quite constant with flapping frequency, increasing slightly from about 60 deg at 3 Hz to about 75 deg at 6 Hz. The CFD analysis by itself predicts that the maximum lift occurs slightly later than the test data show (phase closer to 90 deg, which corresponds to maximum lift at the middle of the downstroke). With the inclusion of the inertial effects, the maximum 1/cycle lift appears to occur slightly earlier than what the test data show.

A comparison of the analysis and test data for the thrust force shows a significant qualitative difference. The test data show a peak in the thrust force amplitude between 5 and 5.5 Hz and a corresponding shift in the phasing of the maximum thrust from −90 (maximum thrust at midstroke) to 0 deg (maximum thrust at stroke reversal). The CFD analysis, on the other hand, shows the amplitude

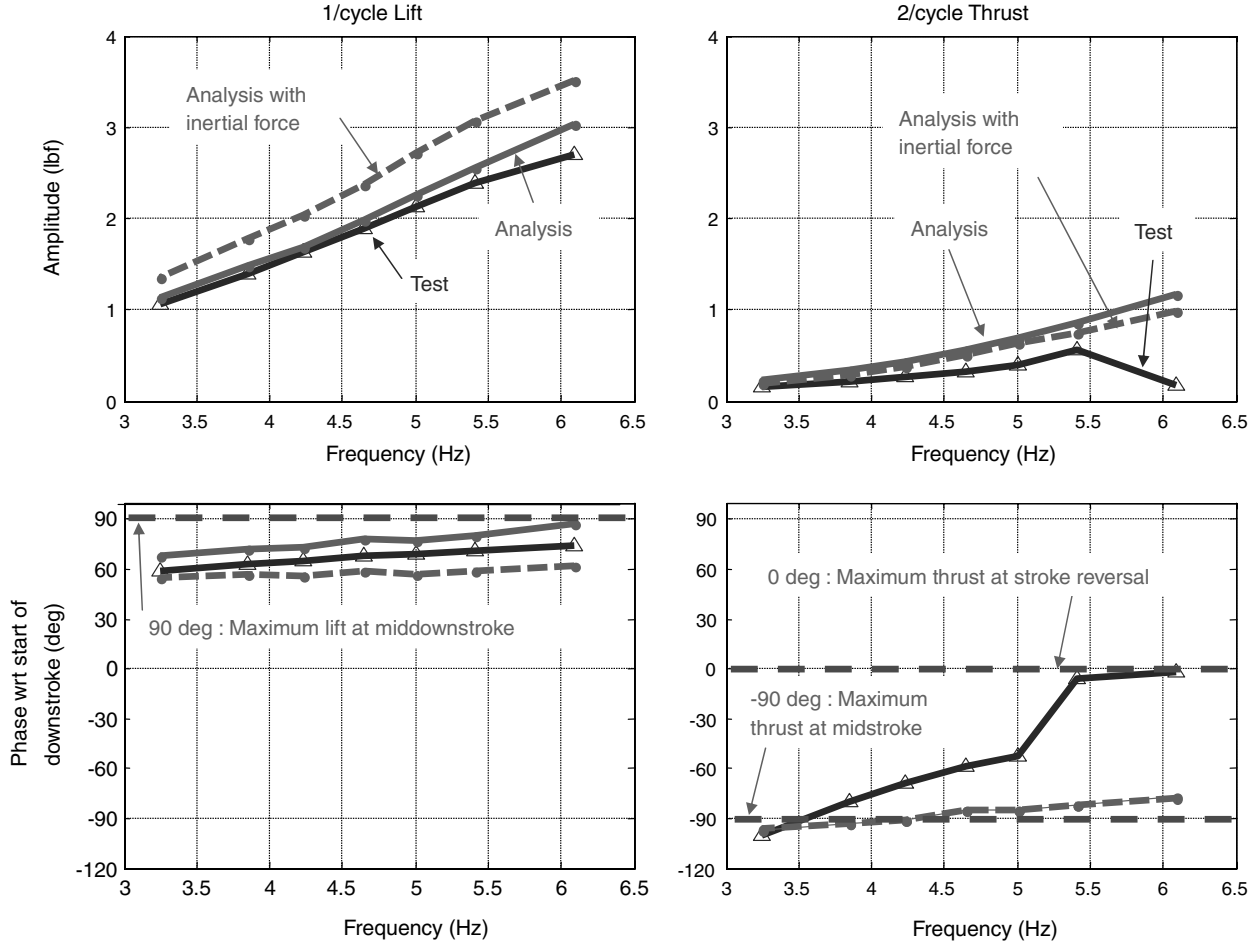

Fig. 26 Comparison of test data and analysis for the harmonic analysis of lift and thrust.

of the thrust force increasing monotonically with frequency and the maximum thrust occurring at around the same phase irrespective of frequency, around the middle of each stroke. The observation that the resonance phenomenon displayed in the test data is not captured by the analysis, even with inclusion of wing inertia forces, seems to indicate that the observed resonance at about 11 Hz originates from some unmodeled components. Further testing is required to confirm this and allow a reliable comparison with the experiment.

IV. Conclusions

This paper presents the development of a CFD methodology for computing aerodynamic loading on flexible flapping wings. The force predictions have been correlated with available experimental data from an ornithopter test, which provides wing surface motions as well as force time history. To model the very large wing deformations encountered during the experiment, a methodology has been devised, implemented, and tested to generate deformed grids that conform to the measured sensor locations.

Although the analytical results correlate satisfactorily with the experiment for low flapping frequencies, significant disagreement exists at higher frequencies, which requires both further experimental and analytical investigation.

This paper demonstrates the capability of the combined flow solver and grid deformation methodology to produce physically meaningful solutions taking into account the flexible wing kinematics. A limited sensitivity study has been conducted, showing convergence of simulation results with respect to grid dimension and time step size.

Flexible flapping wings pose a myriad of complexities for numerical simulations. This study was primarily devoted to the inclusion of high flexibility into a CFD solver and hence investigated only few aspects of this challenging problem. However, the methodology implemented herein opens the possibility for performing detailed investigations in the future, including the analysis of fluid-structure interactions, the effects of turbulence, and the study of transitional flow.

Acknowledgments

This work was performed while the first two authors were employed at the National Institute of Aerospace and was cosupported by a Defense Advanced Research Projects Agency subcontract from Shakti Technologies and the U.S. Army Research Laboratory. The authors would like to acknowledge the Morpheus Laboratory at the National Institute of Aerospace and the NASA Langley Research Center for providing access to experimental data and ornithopter structural properties. Support from the University of Maryland Minta Martin scholarship is also gratefully acknowledged. The authors wish to thank James Baeder, Brandon Bush, and Vinod Lakshminarayanan at the University of Maryland for useful discussions and exchange of code segments. The authors also wish to thank Joseph Conroy at the University of Maryland for his contributions.

References

[1] Eldredge, J. D., "Numerical Simulation of the Fluid Dynamics of 2D Rigid Body Motion with the Vortex Particle Method," *Journal of Computational Physics*, Vol. 221, No. 2, Feb. 2007, pp. 626–648. doi:10.1016/j.jcp.2006.06.038

[2] Young, J., and Joseph, C. S., "Numerical Simulation and Parameter Variation of Insect Wing Motion Based on Dragonfly Hovering," AIAA Paper 2006-38, Jan. 2006.

[3] Toomey, J., and Eldredge, J. D., "Numerical and Experimental Study of the Fluid Dynamics of a Flapping Wing with Low Order Flexibility," *Physics of Fluids*, Vol. 20, July 2008.doi:10.1063/1.2956372

[4] Ramamurthi, R., Sandberg, W., Vaiana, P., Kellog, J., and Cylinder, D., "Computational Fluid Dynamics Study of Unconventional Air Vehicle Configurations," *Aeronautical Journal*, Vol. 109, No. 1097, July 2005, pp. 337–347.

[5] Platzer, M. F., Jones, K. D., Young, J., and Lai, J. C. S., "Flapping-Wing Aerodynamics: Progress and Challenges," *AIAA Journal*, Vol. 46, No. 9, Sept. 2008, pp. 2136–2149. doi:10.2514/1.29263

[6] Viieru, D., Tang, J., Lian, Y., Liu, H., and Shyy, W., "Flapping and Flexible Wing Aerodynamics of Low Reynolds Number Flight Vehicles," AIAA Paper 2006-503, Jan. 2006.

[7] Harmon, R., and Hubbard, J., "Characterization of an Ornithopter Wing," Johns Hopkins Univ. Applied Physics Lab. Paper 5A2, Nov. 2007.

[8] Mittal, R., and Iaccarino, G., "Immersed Boundary Methods," *Annual Review of Fluid Mechanics*, Vol. 37, Jan. 2005, pp. 239–261. doi:10.1146/annurev.fluid.37.061903.175743

[9] Gilmanov, A., and Sotiropoulos, F., "A Hybrid Cartesian/Immersed Boundary Method for Simulating Flows with 3D, Complex Moving Bodies," *Journal of Computational Physics*, Vol. 207, No. 2, Aug. 2005, pp. 457–492. doi:10.1016/j.jcp.2005.01.020

[10] Balaras, E., "Modeling Complex Boundaries Using an External Force Field on Fixed Cartesian Grids in Large-Eddy Simulations," *Computers and Fluids*, Vol. 33, No. 3, March 2004, pp. 375–404. doi:10.1016/S0045-7930(03)00058-6

[11] Batina, J. T., "Unsteady Euler Algorithm with Unstructured Dynamic Mesh for Complex-Aircraft Aerodynamic Analysis," *AIAA Journal*, Vol. 29, No. 3, April 1991, pp. 327–333. doi:10.2514/3.10583

[12] Farhat, C., Degand, C., Koobus, B., and Lesoinne, M., "Torsional Springs for Two-Dimensional Dynamic Unstructured Fluid Meshes," *Computational Methods in Applied Mechanics and Engineering*, Vol. 163, Nos. 1–4, 1998, pp. 231–245.

[13] Loehner, R., and Yang, C., "Improved ALE Mesh Velocities for Moving Bodies," *Communications in Numerical Methods in Engineering*, Vol. 12, 1996, pp. 599–608. doi:10.1002/(SICI)1099-0887(199610)12:10<599::AID-CNM1>3.0.CO;2-Q

[14] Rendall, T. C. S., and Allen, C. B., "Efficient Mesh Motion using Radial Basis Functions with Data Reduction Algorithms," AIAA Paper 2008-305, Jan. 2008.

[15] Liu, X., Qin, N., and Xia, H., "Fast Dynamic Grid Deformation Based on Delaunay Graph Mapping,"*Journal of Computational Physics*, Vol. 211, No. 2, Jan. 2006, pp. 405–423. doi:10.1016/j.jcp.2005.05.025

[16] Cizmas, P., and Gargoloff, J., "Mesh Generation and Deformation Algorithm for Aeroelasticity Simulations," *Journal of Aircraft*, 0021-8669, Vol. 45, No. 3, 2008, pp. 1062–1066. doi:10.2514/1.30896

[17] Rendall, T. C. S., and Allen, C. B., "Unified Fluid-Structure Interpolation and Mesh Motion using Radial Basis Functions," *International Journal for Numerical Methods in Engineering*, Vol. 74, No. 10, 2008, pp. 1519–1559. doi:10.1002/nme.2219

[18] Sitaraman, J., and Baeder, J. D, "On the Field Velocity Approach and Geometric Conservation Law for Unsteady Flow Simulations," AIAA Paper 2003-3835, 2003.

[19] Harmon, R., Grauer, J., Hubbard, J., and Humbert, S., "Experimental Determination of Ornithopter Membrane Wing Shapes Used for Simple Aerodynamic Modeling," AIAA Paper 2008-6237 , Aug. 2008.

[20] Srinivasan, G. R., and Baeder, J. D., "TURNS: A Free-wake Euler/Navier–Stokes Numerical Method for Helicopter Rotors," *AIAA Journal*, Vol. 31, No. 5, 1993, pp. 959–962. doi:10.2514/3.49036

[21] Meakin, R., and Wissink, A. M., "Unsteady Aerodynamic Simulation of Static and Moving Bodies using Scalable Computers," AIAA Paper CP-99-3302, July 1999.

[22] Roe, P. L., "Approximate Riemann Solvers, Parametric Vectors, and Difference Schemes," *Journal of Computational Physics*, Vol. 43, No. 3, 1981, pp. 357–372.

[23] Jameson, A., and Yoon, S., "Lower-Upper Implicit Schemes with Multiple Grids for the Euler Equations," *AIAA Journal*, Vol. 25, No. 7, 1987, pp. 929–935. doi:10.2514/3.9724

[24] Baldwin, B., and Lomax, H., "Thin Layer Approximation and Algebraic Model for Separated Flows," AIAA Paper 1978-257, Jan. 1978.

[25] Spalart, P. R., and Allmaras, S. R., "A One-Equation Turbulence Model for Aerodynamic Flows," AIAA Paper 1992-0439, Jan. 1992.

[26] Sitaraman, J., and Baeder, J. D., "Evaluation of the Wake Prediction Methodologies Used in CFD Based Rotor Airload Computations," AIAA Paper 2006-3472, June 2006.

[27] Sitaraman, J., "CFD-Based Unsteady Aerodynamic Modeling for Rotor Aeroelastic Analysis," Ph.D. Dissertation, Dept. of Aerospace

Engineering, Univ. of Maryland at College Park, College Park, MD, 2003.

[28] Turkel, E., "Preconditioning Techniques for Solving the Incompressible and Low Speed Compressible Equations," *Journal of Computational Physics*, Vol. 72, No. 2, Oct. 1987, pp. 277–298. doi:10.1016/0021-9991(87)90084-2

[29] Gupta, V., "An Investigation of Quad Tilt Rotor Aerodynamics in Helicopter Mode," Ph.D. Dissertation, Dept. of Aerospace Engineering, Univ. of Maryland at College Park, College Park, MD, 2005.

[30] Pandya, S. A, Venkateswaran, S., and Pullium, T., "Implementation of Preconditioned Dual-time Procedures in OVERFLOW," AIAA Paper 2003-0072, Jan. 2003.

[31] Lakshminaryanan, V., "Computational Investigation of Micro-Scale Coaxial Rotor Aerodynamics in Hover," Ph.D. Dissertation, Dept. of Aerospace Engineering, Univ. of Maryland at College Park, College Park, MD, 2009.

[32] Pullium, T., and Chausse, D., "A Diagonal Form of an Implicit Approximate Factorization Algorithm," *Journal of Computational Physics*, Vol. 39, No. 2, Feb. 1981, pp. 347–363. doi:10.1016/0021-9991(81)90156-X